IEEE Access
Multidisciplinary | Rapid Review | Open Access Journal

Received March 31, 2020, accepted April 14, 2020, date of publication April 17, 2020, date of current version May 15, 2020.

Digital Object Identifier 10.1109/ACCESS.2020.2988529

A Bio-Inspired Navigation Strategy Fused Polarized Skylight and Starlight for Unmanned Aerial Vehicles

QINGYUN ZHANG[1], JIAN YANG[1,2,3], XIN LIU[1], AND LEI GUO[1,2,3], (Senior Member, IEEE)

[1]School of Automation Science and Electrical engineering, Beihang University, Beijing 100191, China
[2]Beijing Advanced Innovation Center for Big Data-Based Precision Medicine, School of Medicine and Engineering, Beihang University, Beijing 100191, China
[3]Key Laboratory of Big Data-Based Precision Medicine (Beihang University), Ministry of Industry and Information Technology, Beijing 100191, China

Corresponding authors: Jian Yang (jyangbuaa@126.com) and Lei Guo (lguo@buaa.edu.cn)

This work was supported by the National Natural Science Foundation of China under Grant 61627810, Grant 61751302, and Grant 61973012.

ABSTRACT The migratory animals are capable of traveling long distances by fusing varied information, such as the halteres, the star positions, and the polarization pattern. Motivated by the navigation strategy of migratory animals, a bio-inspired navigation strategy based on polarized skylight, starlight, and halteres is presented in this paper. To enhance the environmental adaptability of the polarization navigation system, a sun vector calculation method tightly fusing the degree of polarization (DoP) and the azimuth of polarization (e-vector) is proposed. By setting the threshold of DoP values of the observation points, the DoP and the e-vector within the threshold range can be selected to deduce the sun position. As such, the robustness and reliability of the sun position can be improved. Concerned with the issue of attitude and heading determination in GNSS-challenged conditions, an integrated navigation strategy combined with polarized light and starlight is proposed. In addition, a Kalman filter is adopted to fuse the navigation data of polarized light, starlight, and inertial sensors. Finally, simulations are conducted to validate the performance of the integrated model. The results illustrated that the proposed navigation strategy is capable of determining the attitude and heading in the scenarios of which the Global Navigation Satellite System (GNSS) is disturbed.

INDEX TERMS Polarized skylight, starlight, navigation strategy, GNSS-challenged condition.

I. INTRODUCTION

A. BACKGROUND

The navigation system is critical for High Altitude Long Endurance Unmanned Aerial Vehicles (HALE UAVs) surveillance, remote sensing, and mapping [1]. In the past few decades, with the requirement of high-precision and real-time, the Strap-down Inertial Navigation System (SINS) integrated with the Global Navigation Satellite System (GNSS) has been commonly applied for HALE UAVs [2], [3]. However, the GNSS is susceptible to electromagnetic interference, and its performance would be degraded in the jamming and spoofing scenarios [4], [5]. The Celestial Navigation System (CNS) is an effective navigation method to compensate for the error of SINS in GNSS-denied conditions [6], [7]. However, its navigation performance is influenced by the number of observable stars. In most cases, being restricted by the observation view of star sensors, only one navigation star can be observed in daytime in the atmosphere [8]. Currently, focusing on the issue of attitude and heading determination of HALE UAVs in GNSS challenged conditions during a long-range journey in daytime, how to develop an autonomous navigation system is a hotspot issue [9].

Many animals are eminent navigators by fusing multiple sensory organs to sense the attitude and heading in their journeys [10]. Arguably, the star position and the magnetic field are the effective compass cues for foraging, homing, and migrating [11], [12]. In the last two decades, a large number of studies have shown that the polarized skylight dominates the heading orientation process in the animals' compass systems. Relevant reports claim that some migratory birds can even use the light cue to calibrate other compass systems [13]. The bio-inspired polarization navigation strategy has show some promising features, including anti-electromagnetic interference and non-accumulation error [14], [15]. Currently, it has attracted considerable attention in the autonomous navigation field.

The associate editor coordinating the review of this manuscript and approving it for publication was Farid Boussaid.

B. RELATED WORKS

Motivated by the polarization navigation mechanism of animals, prosperous progress has been achieved in sensor design, modeling, and calibration [16]–[18]. In addition, to address the challenge of autonomous navigation without GNSS, a series of polarization-based integrated navigation methods have been designed. The research in this field approximately focuses on two aspects:

1) COMBINATION WITH INERTIAL SENSORS

Currently, researches on inertial sensors integrated with polarization compass have drawn growing interest in the autonomous navigation field. For example, the integrated navigation methods combining the Inertial Measurement Unit (IMU) with the polarization sensor are presented in [19]. In their works, a polarization sensor is employed to compensate for the heading accumulated error derived from IMU. The polarization heading is calculated based on the orthogonal relationship between the azimuth of polarization (e-vector) and the sun azimuth. In addition, the accelerometer correction has also been proposed to be used to obtain both attitude and heading information for vehicles [20]. In recent research, a bio-inspired polarization-based attitude and heading reference system (PAHRS) is developed. The three-dimensional polarization heading information can be calculated independently of GNSS correction [21]. However, the aforementioned algorithms are all based on e-vector without considering the information provided by the degree of polarization (DoP). It may be unreliable for UAVs in long-endurance and long-range navigation process.

2) COMBINATION WITH VISUAL SENSORS

To simulate the POL-neuron of desert ants, a bioinspired polarization compass is designed [22]. In combination with panoramic visual sensors and ambient light sensors, a navigation system is developed and is used to mimic the navigation strategy of desert ants [23]. Dragonflies can navigate by fusing multi-sensory organ information. Inspired by this strategy, the biomimetic attitude and heading sensors are designed for UAV navigation and stabilization [24]. To be more specific, a polarization compass is employed to determine heading information, and a biomimetic ocellus is used to the attitude reference of the aircraft. To assist the visual-inertial navigation system (VINS), a camera-based polarization compass is used to compensate for the heading accumulated error of VINS in [25], [26]. The aforementioned studies have attained sound results in attitude and heading determination when GNSS is inapplicable. However, the visual-based approaches have limited applications, especially in unstructured and unknown environments for HALE UAVs.

C. CONTRIBUTION

In this paper, to determine the attitude and heading of HALE UAVs, an autonomous navigation strategy combined with polarized light and starlight is presented. Two key technical issues are considered. The first issue is how to determine the sun vector by fusing the DoP and the e-vector. The second issue is the integration mechanism of the polarization navigation system (PNS) and the Celestial Navigation System (CNS). The main contributions are summarized as follows:

- Concerned with the environmental adaptability of the PNS in HALE UAVs application, a sun vector calculation method is proposed based on the information fusion with the DoP and e-vector. By setting the threshold of the DoP value of the observation point, the corresponding e-vectors in the threshold range can be used to calculate the sun vector. The robustness and reliability of the sun vector can be thereby improved.
- Inspired by the multiple sensory fusion mechanism of migratory animals, an integrated navigation strategy combined with polarized skylight and starlight is presented. In GNSS challenged conditions, the proposed strategy is capable of determining the attitude and heading of HALE UAVs, even in the scenarios with only one navigation star available.

Accordingly, the remainder of this paper is organized as follows. The definition of the reference frames and the sun vector and star vector calculation are presented in section II. On this basis, the attitude and headings solution is given in section III. The SINS/PNS/CNS integrated navigation strategy is established in section IV. In section V, the simulation tests are carried out to validate the effectiveness of the proposed strategy. Finally, the conclusion is drawn in section VI.

II. THE SUN VECTOR AND STAR VECTOR CALCULATION

For some kinds of insects, they can use the polarization vision to sense wide-field polarized skylight to enhance the heading determination ability in complex sky conditions. Inspired by the multidirectional observation mechanism of the insect polarization vision, a bioinspired polarization compass structure is presented in this section.

To mimic the wide field of the compound eye, the bioinspired polarization compass is a hemisphere structure and includes nine polarization sensor units. The polarization sensor units are distributed in an array on the surface of the hemisphere. The structure of the bioinspired polarization compass is shown in Fig. 1. Based on the bioinspired polarization compass, the multiple e-vector information in different directions can be observed. As such, the robustness and reliability of the compass can be enhanced. In what follows, the sun vector calculation method by fusing the DoP and e-vector information is presented. In an attempt to help the readers better comprehend the working principle of the method, the coordinate frames to be used in this paper are presented in Fig. 2.

A. DEFINITION OF THE REFERENCE FRAMES

The **geocentric inertial frame** (**i-frame**) and the **earth frame** (**e-frame**) are common coordinate systems. The detailed definition can be found in [27].

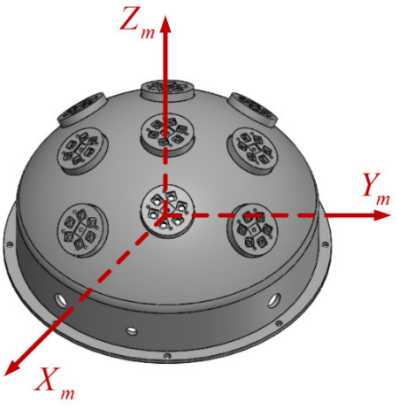

FIGURE 1. The bioinspired polarization compass structure.

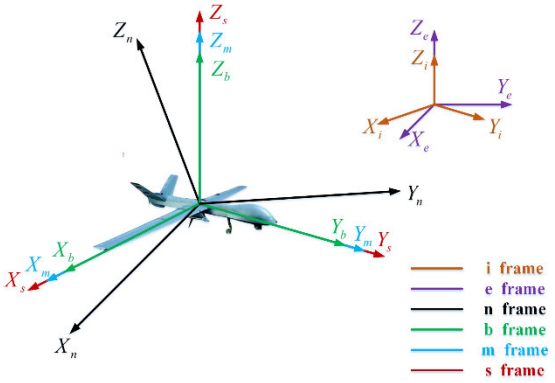

FIGURE 2. The relationship of the coordinate frames.

The **navigation frame (n-frame)** is the geographic coordinate system. The X_n-, Y_n-, and Z_n-axis aligned with the geographic of east, north, and up direction.

The **body frame** (**b-frame**) is the frame fixed on the aircraft. The direction of X_b-, Y_b-, and Z_b-axis are illustrated in Fig. 2.

The **star sensor frame** (**s-frame**) has its origin at the center of the star sensor's image plane with the Z_s-axis perpendicular to the image plane. The X_s-axis and Y_s-axis satisfy the right-hand rule.

The **bioinspired polarization compass frame** (**m-frame**) has its origin at the center of the hemisphere plane. Each polarization sensor unit distributes in an array on the surface of the hemisphere. The X_m-axis is the zero-position direction of the bioinspired polarization compass, the Z_m-axis is aligned with the observation direction of the center bioinspired polarization compass, and the Y_m-axis is perpendicular with the plane formed by the X_m-axis and the Z_m-axis.

In this paper, the star sensor and the bioinspired polarization compass are fixed to the body frame. The star sensor frame and the bioinspired polarization compass frame are considered consistent with the body frame. For the sake of convenience, the symbols represent the attitude transfer matrixes between the frames to be used in this paper can be found in Table 1.

TABLE 1. Symbol representation.

Symbol	Representation
$\boldsymbol{C}_i^b$	attitude transfer matrix between the i-frame and the b-frame
$\boldsymbol{C}_i^e$	attitude transfer matrix between the i-frame and the e-frame
$\boldsymbol{C}_e^n$	attitude transfer matrix between the e-frame and the n-frame
$\boldsymbol{C}_b^n$	attitude transfer matrix between the b-frame and the n-frame
$\boldsymbol{C}_s^b$	attitude transfer matrix between the s-frame and the b-frame

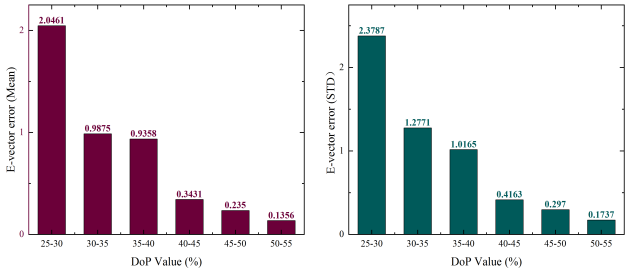

FIGURE 3. (a) The relationship between DoP and the e-vector error (mean). (b) The relationship between DoP and the e-vector error (STD).

B. THE SUN VECTOR CALCULATION METHOD BASED ON DOP AND E-VECTOR FUSION

The polarization pattern distributed across the sky can be expressed as the degree of polarization (DoP) and the azimuth of polarization (e-vector). On the basis of the orthogonal relationships between e-vectors and the sun vector (sun elevation and sun azimuth), the sun vector can be deduced by two separate e-vectors [28]. Although the existing method is able to identify the sun azimuth and sun elevation from the e-vector pattern, it has limitations as follows: 1) the performance of sun vector is restricted by the measurement accuracy of e-vectors. 2) DoP value at the observation point dominates the e-vector error. In polarization vision of insects, the e-vectors can be used to heading orientation only when the measured DoP is larger than a threshold value. To determine the relationship between the DoP value and the e-vector errors, a test has been constructed, and the results are shown in Fig. 3.

It can be seen from the results, to determine the sun vector by using the e-vector pattern, the reliability of the e-vector information should be determined first. Therefore, in this paper, a sun vector calculation method based on the DoP and e-vector information fusion is proposed. By measuring the polarized skylight cues, the DoP (d_i) and e-vector ($\boldsymbol{E}_i^m$) of the i^{th} polarization sensor unit can be calculated by the bioinspired polarization compass.

To determine the relationship between the DoP value and e-vector errors, the outdoor test is constructed, and the test results in Fig. 3 show that when the DoP value less than 30%, the mean value and standard deviation of the e-vector errors

TABLE 2. The sun vector calculation algorithm.

Step 1: obtain the polarization information by the bioinspired polarization compass $\left(\boldsymbol{E}_i^m, d_i\right)$
Step 2: set the DoP threshold d_0 ($d_0 = 30\%$)
Step 3: extract the polarization information $\left(\boldsymbol{E}_i^m, d_i\right)$, $d_0 < d_i < 75\%$
Step 4: set the weight of the $\boldsymbol{S}_{ij}^b$ calculated by the i^{th} and the j^{th} polarization sensor: $\lambda_{ij} = \frac{\left(d_i + d_j\right)}{(k-1)\sum_{i=1}^{k} d_i}, i \neq j$, k is the number of polarization sensor units
Step 5: calculate the sun-vector in the body frame $\mathbf{S}_{sun}^b = \sum \lambda_{ij} \mathbf{S}_{ij}^b$

are larger than 2°. In such cases, we believe that the e-vector cannot meet the heading determination requirements. Hence, in this paper, the DoP threshold (d_0) is set to 30%. In addition, the relevant studies show that the maximum degree of polarization across the sky is no larger than 75%, even in clear sky conditions [29]. Hence, the threshold of the DoP value of the observation points should satisfy as follows.

$$d_0 < d_i < 75\% \tag{1}$$

Finally, set the weight of the distribution coefficient matrix of e-vectors:

$$\boldsymbol{\lambda}_{ij} = \frac{\left(d_i + d_j\right)}{(k-1)\sum_{i=1}^{k} d_i}, \quad i \neq j, \ \sum \boldsymbol{\lambda}_{ij} = \boldsymbol{I} \tag{2}$$

where k is the number of polarization sensor units.

Based on the orthogonal relationship between the sun vector and e-vectors, the sun vector in the b-frame ($\boldsymbol{S}_{ij}^b$) can be calculated as:

$$\boldsymbol{S}_{ij}^b == \frac{\boldsymbol{E}_i^b \otimes \boldsymbol{E}_j^b}{\sin\langle \boldsymbol{E}_i^b, \boldsymbol{E}_j^b \rangle} = \frac{\boldsymbol{C}_{mi}^b \boldsymbol{E}_i^m \otimes \boldsymbol{C}_{mj}^b \boldsymbol{E}_j^m}{\sin\langle \boldsymbol{E}_i^m, \boldsymbol{E}_j^m \rangle} \tag{3}$$

where $\boldsymbol{C}_{mi}^b$ is the attitude transfer matrix between the m-frame and the b-frame of the i^{th} polarization sensor unit, $\langle \boldsymbol{E}_i^b, \boldsymbol{E}_j^b \rangle$ are the angle between $\boldsymbol{E}_i^b$ and $\boldsymbol{E}_j^b$, and $\langle \boldsymbol{E}_i^m, \boldsymbol{E}_j^m \rangle$ are the angles between $\boldsymbol{E}_i^m$ and $\boldsymbol{E}_j^m$;

In combination with the Eqs. (2) and (3), the sun vector in the b-frame can be calculated as follows.

$$\boldsymbol{S}_{sun}^b = \sum \lambda_{ij} \boldsymbol{S}_{ij}^b \tag{4}$$

The algorithm can be summarized in Table 2:

Equation (4) expressed the sun vector fused with the DoP and e-vector. Distinguished from [28], [30], the proposed method takes into account the influence of environmental factors on the sun vector calculation performance. By making full use of the polarized skylight information, the accuracy and robustness of the sun vector calculation can be consequently improved.

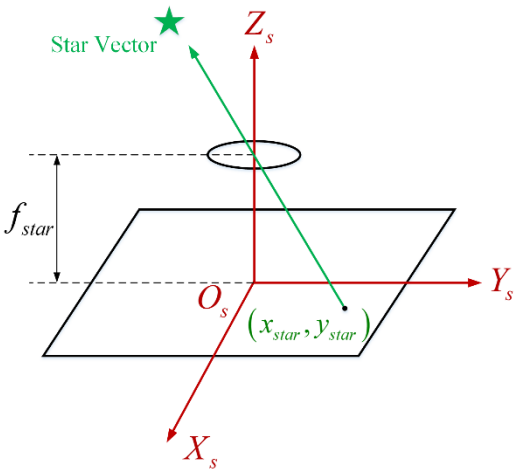

FIGURE 4. The position of the star vector in the s-frame.

C. STARLIGHT INFORMATION ACQUISITION AND STAR VECTOR CALCULATION

When the HALE UAV flies in the atmosphere, the performance of the star sensor is affected by environmental interference and background noise. It has an adverse effect on the observation of multiple stars. Thus, the narrow field star sensor is used to capture the navigation star information for HALE UAVs application. When the star sensor works, a pre-selected one or more unique stars are loaded to the navigation star database. Driven by the tracking device, the optical axis of the star sensor is always aligned with the target star aided by the position and attitude information from the previous moment. The star sensor acquires the star map point in the s-frame as shown in Fig. 4. In combination with the transformation matrix between s-frame and b-frame, the star vector ($\boldsymbol{V}_{star}^b$) in the b-frame can be obtained from the star map point in the s-frame, as shown below:

$$\boldsymbol{V}_{star}^b = \boldsymbol{C}_s^b \boldsymbol{V}_{star}^s = \boldsymbol{C}_s^b \frac{\begin{bmatrix} -x_{star} & -y_{star} & f_{star} \end{bmatrix}^T}{\sqrt{x_{star}^2 + y_{star}^2 + f_{star}^2}} \tag{5}$$

where (x_{star}, y_{star}) is the coordinate of the star vector in the s-frame; f_{star} is the focal length of the star sensor optical lens.

Accordingly, the star vector in the b-frame can be represented as:

$$\boldsymbol{V}_{star}^b = \begin{bmatrix} \cos A_{star}^b \cos H_{star}^b & \sin A_{star}^b \cos H_{star}^b & \sin H_{star}^b \end{bmatrix}^T \tag{6}$$

where A_{star}^b, H_{star}^b are the star azimuth and elevation in the b-frame, respectively.

III. THE ATTITUDE AND HEADING DETERMINATION BASED ON SUN VECTOR AND STAR VECTOR

The sun vector ($\boldsymbol{S}_{sun}^b$) and the star vector ($\boldsymbol{V}_{star}^b$) in the b-frame are obtained in the above section. Combining with the right ascension and declination of the celestial body from the astronomical ephemeris and time, the sun vector ($\boldsymbol{S}_{sun}^i$) and

the star vector ($\boldsymbol{V}^i_{star}$) in the i-frame can be represented as:

$$\begin{cases} \boldsymbol{S}^i_{sun} = \left[\cos\alpha_{sun}\cos\delta_{sun} \quad \sin\alpha_{sun}\sin\delta_{sun} \quad \sin\delta_{sun}\right]^T \\ \boldsymbol{V}^i_{star} = \left[\cos\alpha_{star}\cos\delta_{star} \quad \sin\alpha_{star}\sin\delta_{star} \quad \sin\delta_{star}\right]^T \end{cases} \tag{7}$$

where α_{sun} and δ_{sun} are the right ascension and declination of the sun, and α_{star} and δ_{star} are the right ascension and declination of the star, respectively. The astronomical ephemeris of the sun and the star is almost constant in a short time. Time information is provided by the clock module integrated into the navigation system of UAVs.

In combination with Eq. (7) and the attitude transfer matrix between the i-frame and the b-frame, the sun vector and the star vector in the b-frame can be illustrated as:

$$\begin{cases} \boldsymbol{S}^b_{sun} = \boldsymbol{C}^b_i \boldsymbol{S}^i_{sun} \\ \boldsymbol{V}^b_{star} = \boldsymbol{C}^b_i \boldsymbol{V}^i_{star} \end{cases} \tag{8}$$

In what follows, to determine the attitude and heading based on the polarized skylight and starlight information, two orthogonal coordinate frames to be used in this paper are presented, which are constructed by the sun vectors and star vectors in the i-frame and the b-frame.

In the i-frame, based on the sun vector and star vector provided by the astronomical ephemeris of the sun and the navigation star, an orthogonal coordinate frame is established as follows:

$$\boldsymbol{F}^i_{ref} = \begin{bmatrix} \boldsymbol{X}^i_{ref} & \boldsymbol{Y}^i_{ref} & \boldsymbol{Z}^i_{ref} \end{bmatrix}^T \tag{9}$$

where

$$\begin{cases} \boldsymbol{X}^i_{ref} = \boldsymbol{S}^i_{sun} \\ \boldsymbol{Y}^i_{ref} = \dfrac{\boldsymbol{S}^i_{sun} \otimes \boldsymbol{V}^i_{star}}{\left\| \boldsymbol{S}^i_{sun} \otimes \boldsymbol{V}^i_{star} \right\|} \\ \boldsymbol{Z}^i_{ref} = \boldsymbol{X}^i_{ref} \otimes \boldsymbol{Y}^i_{ref} \end{cases} \tag{10}$$

Similarly, in the b-frame, the orthogonal coordinate frame is established based on the measurement of the sun vector and star vector, and the corresponding frame is expressed as:

$$\boldsymbol{F}^b_{ref} = \begin{bmatrix} \boldsymbol{X}^b_{ref} & \boldsymbol{Y}^b_{ref} & \boldsymbol{Z}^b_{ref} \end{bmatrix}^T \tag{11}$$

where

$$\begin{cases} \boldsymbol{X}^b_{ref} = \boldsymbol{S}^b_{sun} \\ \boldsymbol{Y}^b_{ref} = \dfrac{\boldsymbol{S}^b_{sun} \otimes \boldsymbol{V}^b_{star}}{\left\| \boldsymbol{S}^b_{sun} \otimes \boldsymbol{V}^b_{star} \right\|} \\ \boldsymbol{Z}^b_{ref} = \boldsymbol{X}^b_{ref} \otimes \boldsymbol{Y}^b_{ref} \end{cases} \tag{12}$$

Based on Eq. (8) and Eq. (12), the three components of $\boldsymbol{F}^b_{ref}$ can be expressed as follows.

$$\begin{cases} \boldsymbol{X}^b_{ref} = \boldsymbol{C}^b_i \boldsymbol{X}^i_{ref} \\ \boldsymbol{Y}^b_{ref} = \dfrac{\boldsymbol{S}^b_{sun} \otimes \boldsymbol{V}^b_{star}}{\left\| \boldsymbol{S}^b_{sun} \otimes \boldsymbol{V}^b_{star} \right\|} = \dfrac{\boldsymbol{C}^b_i \boldsymbol{S}^i_{sun} \otimes \boldsymbol{C}^b_i \boldsymbol{V}^i_{star}}{\left\| \boldsymbol{C}^b_i \boldsymbol{S}^i_{sun} \otimes \boldsymbol{C}^b_i \boldsymbol{V}^i_{star} \right\|} = \boldsymbol{C}^b_i \boldsymbol{Y}^i_{ref} \\ \boldsymbol{Z}^b_{ref} = \boldsymbol{X}^b_{ref} \otimes \boldsymbol{Y}^b_{ref} = \boldsymbol{C}^b_i \boldsymbol{X}^i_{ref} \otimes \boldsymbol{C}^b_i \boldsymbol{Y}^i_{ref} = \boldsymbol{C}^b_i \boldsymbol{Z}^i_{ref} \end{cases} \tag{13}$$

TABLE 3. The attitude and heading calculation algorithm.

Step 1: input the celestial body information: $\boldsymbol{S}^b_{sun}, \boldsymbol{V}^b_{star}, \boldsymbol{S}^i_{sun}, \boldsymbol{V}^i_{star}$
Step 2: construct the coordinate frame: $\boldsymbol{F}^b_{ref}, \boldsymbol{F}^i_{ref}$
Step 3: calculate the transfer matrix: $\boldsymbol{C}^b_i = \boldsymbol{F}^b_{ref}(\boldsymbol{F}^i_{ref})^{-1}$
Step 4: establish the transformation relationship: $\boldsymbol{C}^n_b = \boldsymbol{C}^n_e \boldsymbol{C}^e_i \boldsymbol{C}^i_b$
Step 5: calculate the attitude transfer matrix: $\boldsymbol{C}^n_b = \boldsymbol{R}_z(\psi)\boldsymbol{R}_x(\theta)\boldsymbol{R}_y(\gamma)$
Step 6: calculate the attitude and heading: θ , γ , and ψ

The relationship between the $\boldsymbol{F}^b_{ref}$ and $\boldsymbol{F}^i_{ref}$ can be represented as:

$$\boldsymbol{F}^b_{ref} = \boldsymbol{C}^b_i \boldsymbol{F}^i_{ref} \tag{14}$$

Based on Eq. (14), the attitude transfer matrix between the i-frame and b-frame can be determined by fusing the polarized skylight and starlight information. In addition, the attitude transfer matrix between the b-frame and the n-frame can be denoted as:

$$\boldsymbol{C}^n_b = \boldsymbol{C}^n_e \boldsymbol{C}^e_i \boldsymbol{C}^i_b = \boldsymbol{R}_z(\psi)\boldsymbol{R}_x(\theta)\boldsymbol{R}_y(\gamma) \tag{15}$$

where θ, γ, and ψ are the pitch, roll, and heading of the system, $\boldsymbol{R}_x(\theta)$, $\boldsymbol{R}_y(\gamma)$, and $\boldsymbol{R}_z(\psi)$ are the attitude transfer matrixes of the pitch, roll, and heading, respectively. The expression of $\boldsymbol{R}_x(\theta)$, $\boldsymbol{R}_y(\gamma)$, and $\boldsymbol{R}_z(\psi)$ can be found in the appendix.

Then the attitude and heading of the system can be obtained as:

$$\begin{cases} \gamma_m = \arctan(-C_{3,1}/C_{3,3}) \\ \theta = \arcsin C_{3,2} \\ \psi_m = \arctan(-C_{1,2}/C_{2,2}) \end{cases} \tag{16}$$

where $C_{i,j}$ is the element with the subscript (i, j) in the attitude transfer matrix $\boldsymbol{C}^n_b$. The detailed expression of roll γ and the heading ψ can be found in the appendix.

Then, Eq. (16) shows the attitude and heading of HALE UAVs provided by the integrated navigation strategy. With the aid of PNS, the HALE UAVs are capable of determining the attitude and heading with only one star available.

The algorithm steps are summarized as Table 3:

IV. SINS/PNS/CNS INTEGRATED NAVIGATION SYSTEM MODELING

The attitude and heading are measured by fusing the polarized skylight and starlight information in Section III. On this basis, an integration navigation model combined with INS, PNS, and CNS is established in this section. The system information fusion architecture is illustrated in Fig. 5.

According to the error model of SINS, the state model can be expressed as (see e.g. [27] and references therein):

$$\dot{\boldsymbol{x}}(t) = \boldsymbol{F}(t)\boldsymbol{x}(t) + \boldsymbol{G}(t)\boldsymbol{w}(t) \tag{17}$$

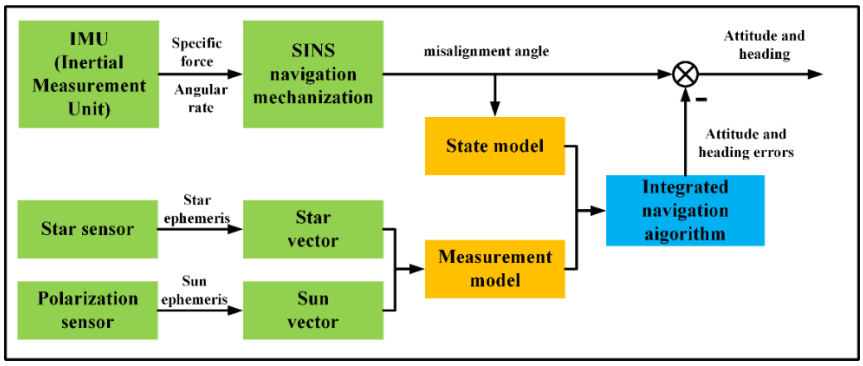

FIGURE 5. The SINS/PNS/CNS integrated model.

where

$$\boldsymbol{x}(t) = [\,\phi^T \quad \delta V^T \quad \delta P^T \quad \varepsilon^T \quad \nabla^T\,]^T \tag{18}$$

$\phi = \left[\,\phi_E \;\; \phi_N \;\; \phi_U\,\right]^T$ are the misalignment angles of SINS;
$\delta V = \left[\,\delta V_E \;\; \delta V_N \;\; \delta V_U\,\right]^T$ are the velocity errors of SINS;
$\delta P = \left[\,\delta L \;\; \delta\lambda \;\; \delta h\,\right]^T$ are the position errors of SINS;
$\varepsilon = \left[\,\varepsilon_x \;\; \varepsilon_y \;\; \varepsilon_z\,\right]^T$ are the constant drifts of gyroscopes;
$\nabla = \left[\,\nabla_x \;\; \nabla_y \;\; \nabla_z\,\right]^T$ are the biases of accelerometers;
$\boldsymbol{F}(t)$ is the state matrix;
$\boldsymbol{G}(t)$ is the system noise matrix;
$\boldsymbol{w}(t)$ is the white noise of gyroscopes and accelerometers.

In this paper, the measurement value ($z(t)$) of the SINS/PNS/CNS integrated navigation system is the attitude angle and heading deviation ($\Delta\theta$, $\Delta\gamma$, $\Delta\psi$), which is the difference between the attitude angle calculated by the sun vector and the star vector and the attitude angle calculated by the SINS. The relationship between the attitude and heading angle deviation and the misalignment angle is shown as:

$$\begin{cases} \Delta\theta = -\cos\psi_s\phi_E - \sin\psi_s\phi_N \\ \Delta\gamma = \dfrac{\sin\psi_s}{\cos\theta_s}\phi_E - \dfrac{\cos\psi_s}{\cos\theta_s}\phi_N \\ \Delta\psi = -\dfrac{\sin\theta_s\sin\psi_s}{\cos\theta_s}\phi_E + \dfrac{\sin\theta_s\cos\psi_s}{\cos\theta_s}\phi_N - \phi_U \end{cases} \tag{19}$$

According to Eq. (19), the system measurement model can be expressed as.

$$\boldsymbol{z}(t) = \boldsymbol{H}(t)\boldsymbol{x}(t) + \boldsymbol{v}(t) \tag{20}$$

where $\boldsymbol{v}(t)$ is the measurement noise of the polarization sensor and the star sensor. The expression of $\boldsymbol{z}(t)$ and $\boldsymbol{H}(t)$ can be found in the appendix.

In this paper, the system noises and measurement noises are treated as Gaussian white noise. A Kalman filter is used to fuse the navigation information measured by polarization sensor, the star sensor, and INS. The parameter settings of the Kalman filter are selected by sensors' specifications. The parameters of P0 matrix is determined by the initial attitude, velocity, and position errors of the system and the initial bias error of gyroscopes and accelerometers. The parameters of Q matrix are the known covariance of the random walk of gyroscopes and accelerometers. In addition, the parameters of R matrix can be determined by the accuracy of the polarization sensor and star sensor. The Kalman filter implemented can be found in [27].

The integrated navigation strategy based on polarized skylight, starlight, and SINS is proposed. As compared with the existing methods, the strategy can provide the attitude and heading for HALE UAVs independent of GNSS correction.

V. SIMULATION AND DISCUSSION

A. VERIFICATION OF THE SUN VECTOR CALCULATION METHOD BASED ON THE DOP AND E-VECTOR

To verify the accuracy of the proposed sun vector calculation method, the simulation experiments are conducted in this subsection. In the simulation, the location of the aircraft is set at (40°N, 116° E), and the test time is set on March 8th, 2019 (from 10:00 Am to 11:00 Am). The DoP and e-vector information are generated by the Rayleigh scattering model. In addition, the threshold of the DoP value is set in the interval from 30% to 75%. According to the quantitative analysis results between the e-vector errors and the DoP value (as shown in Fig. 3), the e-vector error is set to 0.6° when the DoP value is less than 30%, and the e-vector error is set to 0.1° when the DoP value is greater than 50%. To evaluate the performance of the proposed sun calculation method fused the DoP and e-vector information, the sun azimuth and sun elevation provided by the sun astronomical ephemeris are employed as the reference. The traditional sun calculation method can be found in [28]. The simulation results of the sun azimuth and sun elevation calculated by the proposed algorithm and the traditional algorithm are shown in Figs. 6-8.

In Fig. 6, we can see that the sun azimuth (the green curve) provided by the reference has changed from −42.25° to −74.54° during the test time. It can be seen that both the sun azimuth calculated by the proposed algorithm (the blue curve) and the traditional algorithm (the red curve) can well track the reference. However, the sun azimuth calculated by the traditional algorithm presents a significant fluctuation than the proposed algorithm.

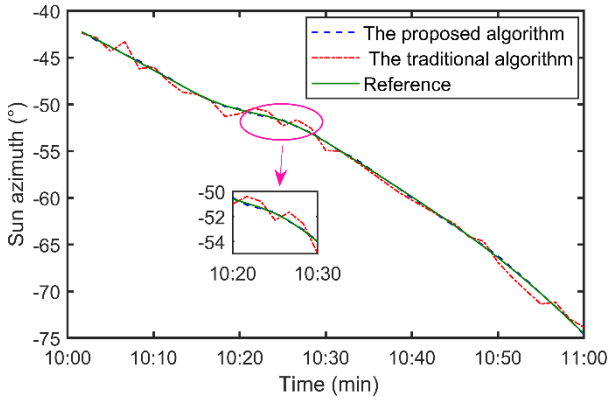

FIGURE 6. Comparison of the sun azimuth.

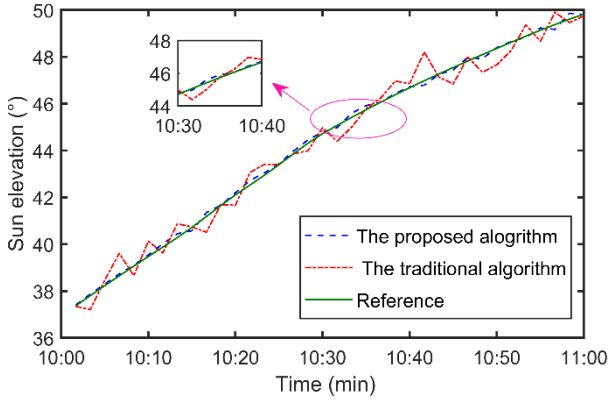

FIGURE 7. Comparison of the sun elevation.

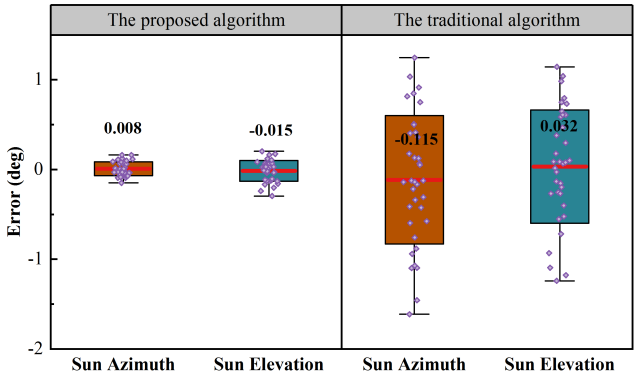

FIGURE 8. Comparison of the sun azimuth and elevation error.

In Fig. 7, we can see that the sun elevation (the green curve) provided by the reference has changed from 37.37° to 49.81° during the test time. It can be seen that both the sun elevation calculated by the proposed algorithm (the blue curve) and the traditional algorithm (the red curve) can well track the reference. However, the sun elevation calculated by the traditional algorithm has a significant fluctuation than the proposed algorithm.

The statistical results of the sun azimuth and sun elevation are shown in Fig. 8. We can see that the sun azimuth mean error of the proposed algorithm is 0.008°, compared with the sun azimuth mean error 0.115° of the traditional algorithm, the mean error of the sun azimuth is reduced by 93.04%. Similarly, the sun elevation mean error of the proposed algorithm is 0.015°, compared with the sun elevation mean error 0.032° of the traditional algorithm, the mean error of the sun elevation is reduced by 53.10%. In addition, the error distribution of sun azimuth and sun elevation of the proposed algorithm has fewer fluctuations than the traditional algorithm.

From the above results, we can see that the traditional algorithm has a poor accuracy than the proposed algorithm without consideration of the influence of the DoP, especially in the scenarios when the DoP value is lower than a certain threshold. The main reason is that the e-vector used in the traditional algorithm has a large error. When calculating the sun azimuth and elevation, the e-vector with large errors will be introduced into the traditional algorithm. However, when considering the threshold of the DoP value, we can choose the e-vector with small errors based on the threshold of the DoP value. The e-vectors with higher accuracy will be used to calculate the sun azimuth and elevation. Hence, the proposed algorithm can improve the accuracy and robustness of sun position calculation.

B. VERIFICATION OF THE SINS/PNS/CNS INTEGRATED MODEL

To verify the effectiveness and anti-interference ability of the SINS/PNS/CNS integrated model, two simulation scenarios are conducted in this section: 1) The aircraft maneuvers flight without external interference. 2) The aircraft maneuvers flight in the electromagnetic interference environment. The simulated trajectory data are generated by trajectory generator. The polarization data are generated based on the Rayleigh scattering model, and the star vector data are generated based on the ephemeris.

1) SIMULATION CONDITIONS WITHOUT EXTERNAL INTERFERENCE

When the aircraft works in the atmosphere in daytime, generally, only the brightest stars are visible. Considering this scenario, the single-star mode is used in the following simulation. The maneuvering flight process of the aircraft includes turning, climbing, diving, and leveling. The flight path is shown in Fig. 9. The flight state is shown in Table 4.

The initial position of the aircraft is 40°N, 116° E, and 10,000 m in height. The initial speed is 300 m/s, and the heading is in the east direction. The pitch and roll are both set to 0°. A medium accuracy inertial navigation system is used, in which the gyro bias stability is 1.0°/*h*, and the angular random walk is $0.5^{\circ}/\sqrt{h}$. The accelerometer bias stability is 0.5 mg, and the velocity random walk is $0.25m/s/\sqrt{h}$. The output frequency of the inertial device is 50 Hz. The output frequency of the polarization sensor and the star sensor are both 1 Hz. The measurement accuracy of the polarization sensor and the star sensor is 0.1°. The details of the sensor parameter are shown in Table 5.

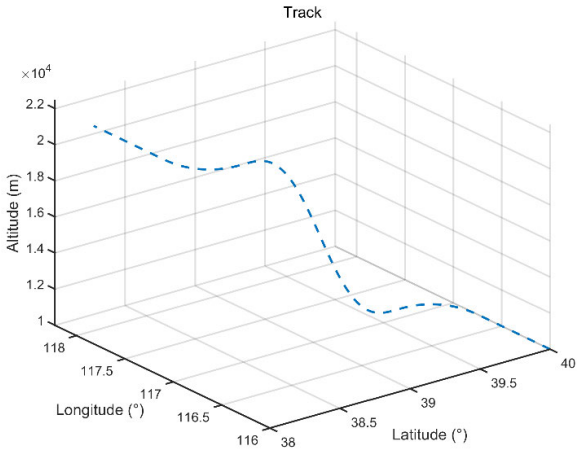

FIGURE 9. Simulation track diagram.

TABLE 4. The flight state of the aircraft.

No.	Time(s)	Variable of Heading(°)	Variable of Pitch(°)	Variable of Roll(°)
1	0-600	0	0	0
2	600-1200	-90	0	11.36
3	1200-1800	0	10	0
4	1800-2400	0	-10	0
5	2400-3000	90	0	-11.36
6	3000-3600	0	0	0

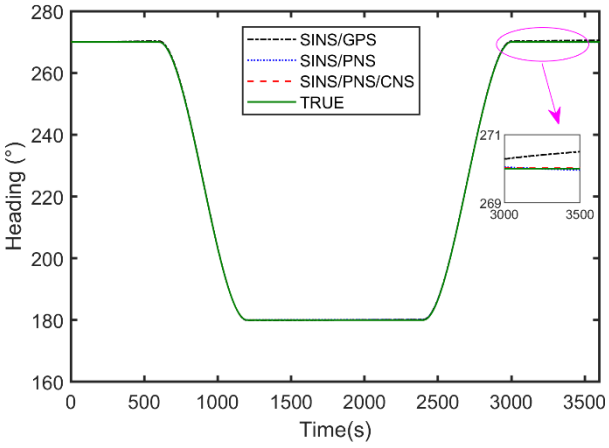

FIGURE 10. Comparison of the heading.

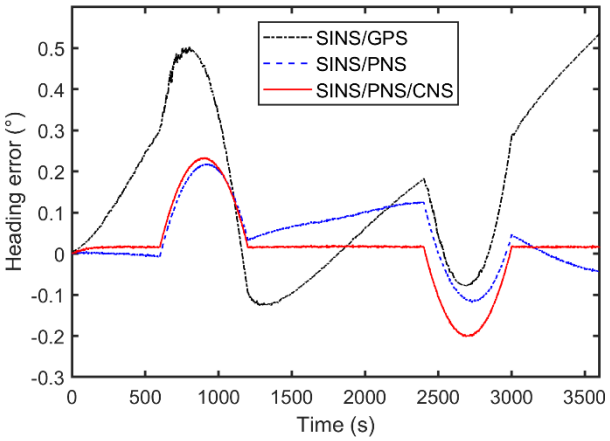

FIGURE 11. Comparison of the heading error.

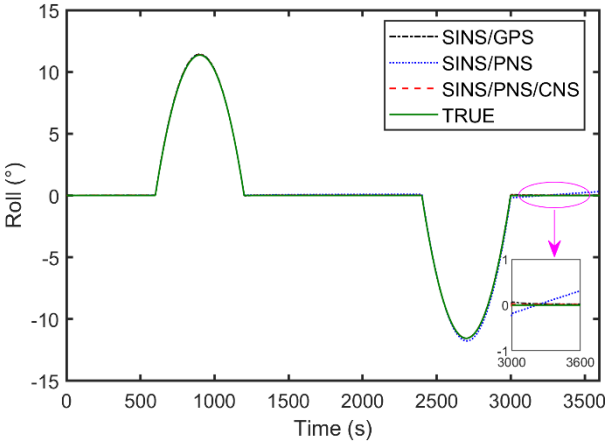

FIGURE 12. Comparison of the roll.

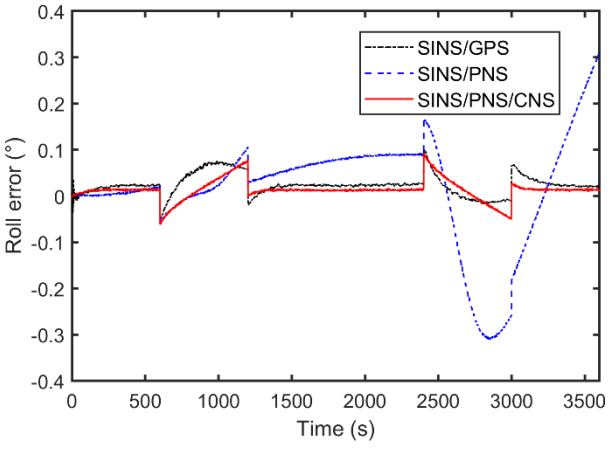

FIGURE 13. Comparison of the roll error.

The system simulation time is 3600s. The navigation performance of the SINS/PNS/CNS integrated model, the SINS/GPS integrated model, and the SINS/PNS integrated model is compared as follows. The simulation results are shown in Figs. 10-15.

Figs. 10-11 illustrate the simulation results of the heading information of the three integrated models. Fig. 10 shows that the heading obtained by each integrated model can track the theoretical value which is generated by the trajectory generator. However, the SINS/GPS integrated model has the worst tracking performance compared with the other two integrated models. From Fig. 11, we can see that when the aircraft works in a maneuver flight (600s-3000s), the heading error of the SINS/GPS integrated model fluctuates greatly and

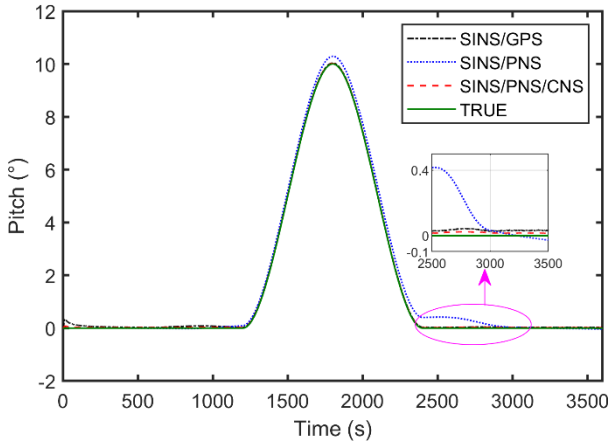

FIGURE 14. Comparison of the pitch.

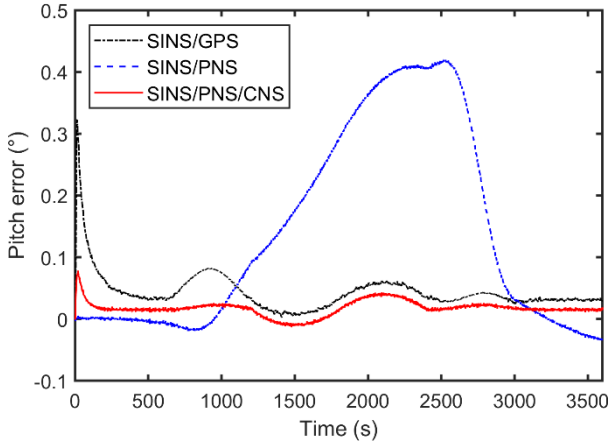

FIGURE 15. Comparison of the pitch error.

TABLE 5. Sensor features.

Sensors	Features
Polarization sensor	Angular accuracy: 0.1° (1σ) Output frequency: 1 Hz
Star sensor	Angular accuracy: 0.1° (1σ) Output frequency: 1 Hz
Gyroscope	Bias stability: 1°/h Angular random walk: $0.5^{\circ}/\sqrt{h}$ Output frequency: 50 Hz
Accelerometer	Bias stability: 0.5 mg Velocity random walk: $0.25m/s/\sqrt{h}$ Output frequency: 50 Hz

has a divergent trend. The heading error of the SINS/PNS integrated model has small-scale fluctuations. When the aircraft works in a stable state (3000s-3600s), it does not converge to the vicinity of zero. However, the heading error of the SINS/PNS/CNS integrated model remains stable continuously. When the aircraft works in a stable state (3000s-3600s), it quickly converges to the vicinity of zero.

Figs. 12-13 illustrate the simulation results of the roll information of the three integrated models. Fig. 12 displays

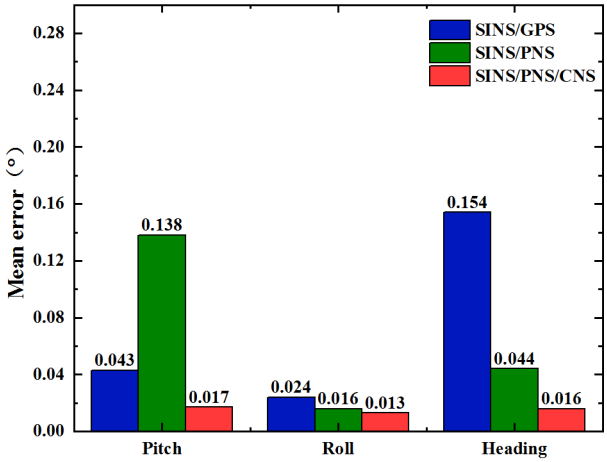

FIGURE 16. Comparison of the mean value of the attitude and heading error.

that the roll obtained by each integrated model can track the theoretical value. However, the SINS/PNS integrated model gives the worst tracking performance compared with the other two integrated models. From Fig. 13, we can see that when the roll of the aircraft changes (600s-1200s, 2400s-3000s), the roll error of the SINS/PNS integrated model fluctuates greatly, having a divergent trend. The other two integrated models have fewer fluctuations in the roll error. When the aircraft works in a stable state (3000s-3600s), the roll error of the SINS/PNS/CNS integrated model converges to the vicinity of zero.

Figs. 14-15 illustrate the simulation results of the pitch information of the three integrated models. Fig. 14 displays that the pitch obtained by each integrated model can track the theoretical value. However, the SINS/PNS integrated model gives the worst tracking performance compared with the other two integrated models. From Fig. 15, we can see that when the pitch of the aircraft changes (1200s-2400s), the pitch error of the SINS/PNS integrated model fluctuates greatly, having a divergent trend. The other two integrated models have small-scale fluctuations in the pitch error. When the aircraft works in a stable state (3000s-3600s), the pitch error of the SINS/PNS/CNS integrated model converges to the vicinity of zero.

The mean value and standard deviation of the attitude and heading error of the three integrated models are shown in Figs. 16-17.

It can be observed from Fig. 16 that the mean value of pitch error derived from the SINS/PNS/CNS integrated model is 0.017°. When comparing to the mean value 0.138° of the SINS/PNS integrated model, the error is reduced by 87.7%. In comparison to the mean value 0.043° of the SINS/GPS integrated model, the error is reduced by 60.5%. The mean value of roll error derived from the SINS/PNS/CNS integrated model and the SINS/PNS integrated model has an equivalent accuracy of 0.013° and 0.016°. Compared with the mean value 0.024° of the SINS/GPS integrated model,

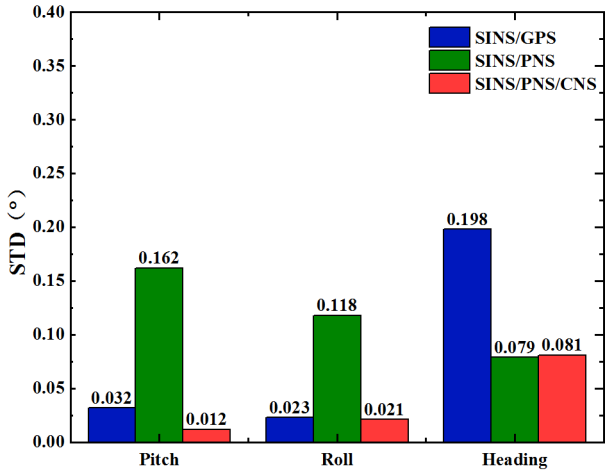

FIGURE 17. Comparison of the standard deviation value of the attitude and heading error.

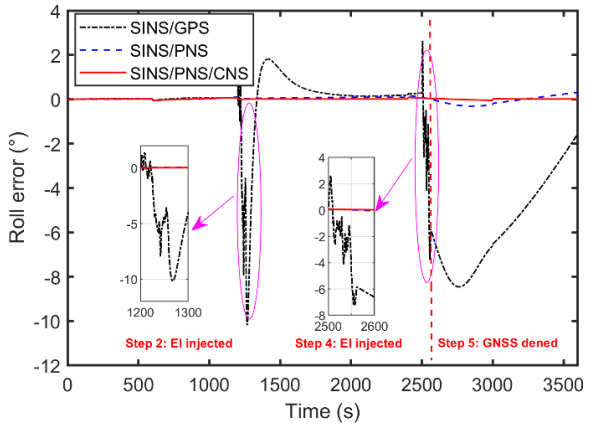

FIGURE 18. Comparison of the roll error.

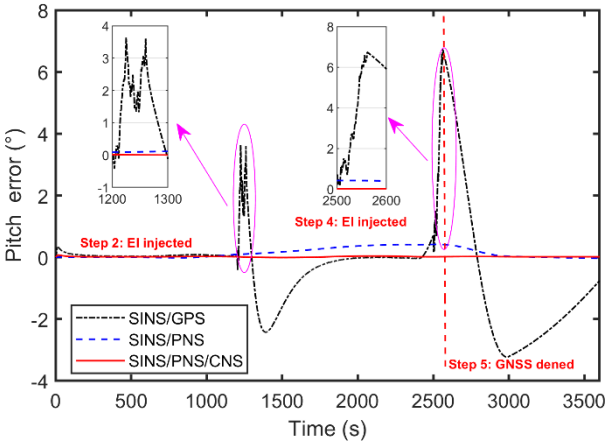

FIGURE 19. Comparison of the pitch error.

the error is reduced by 45.8% and 33.3%, respectively. In the aspect of the heading error correction, the mean value of heading error of the SINS/PNS/CNS integrated model is 0.016°. In contrast to the mean value of the SINS/GPS integrated model 0.154°, the error is reduced by 89.6%. In contrast to the mean value 0.044° of the SINS/PNS integrated model, the error is reduced by 63.6%.

It can be observed from Fig. 17 that the standard deviation of the pitch error derived from the SINS/PNS/CNS integrated model is 0.012°. When comparing to the standard deviation value 0.032° of the SINS/GPS integrated model, the error is reduced by 62.5%. In comparison to the standard deviation value 0.162° of the SINS/PNS integrated model, the error is reduced by 92.6%. The standard deviations of the roll error correction derived from the SINS/PNS/CNS integrated model and the SINS/GPS integrated model have an equivalent accuracy of 0.021° and 0.023°. In contrast to the standard deviation value 0.118° of the SINS/PNS integrated model, the error is reduced by 82.2% and 80.5%. In terms of the heading error correction, the standard deviations of the SINS/PNS/CNS integrated model and the SINS/PNS integrated model have an equivalent accuracy of 0.081° and 0.079°. In contrast to the standard deviation value 0.198° of the SINS/GPS integrated model, the error is reduced by 59.1% and 60.1%, respectively.

From the above results, we can see that the SINS/PNS integrated model has a poor correction capability of the pitch errors and the roll errors. Though the heading errors are corrected to some extent, they do not converge to the vicinity of zero when the aircraft enters the uniform motion state. The heading errors maintain divergence slowly. While the SINS/PNS/CNS integrated model has a better correction capability of the attitude and heading errors. In the uniform motion state, the attitude and heading errors fast converge to the vicinity of zero. It can be attributed to the using of a single vector by the SINS/PNS integrated model. However, the attitude measurement model based on a single vector has at least a one-dimensional unobservable modality when the vehicle is stationary or uniform linear motion. When the polarized light and starlight are introduced to the measurement model, the attitude and heading errors of the integrated model become observable. The estimation of the attitude and heading quickly converges to the vicinity of the theoretical value.

2) VALIDATION IN THE CASE OF ELECTROMAGNETIC INTERFERENCE

When the HALE UAVs perform special tasks, they usually work in the electromagnetic interference environments, and even the GNSS denied environments. In this subsection, the simulation conditions are consistent with the above subsection, except that the electromagnetic interference is imposed [31]. The progress of electromagnetic interference is shown in Table 6. The attitude error curves of the three integrated models are shown in Figs. 18-20.

It can be observed from Figs. 18-20 that the three integrated models are relatively stable at step 1 (0s-1200s), because there is no disturbance imposed. Note that at step 2 (1200s-1260s) and step 4 (2500s-2560s), it can be seen

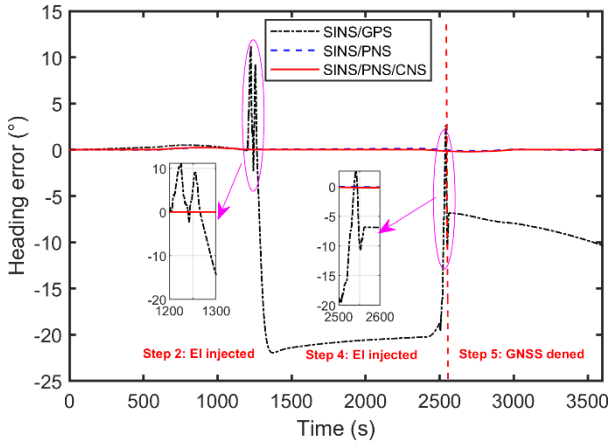

FIGURE 20. Comparison of the heading error.

TABLE 6. Electromagnetic interference performance test steps.

Steps	Time（s）	Electromagnetic interference
1	0-1200	no
2	1200-1260	imposed
3	1260-2500	no
4	2500-2560	imposed
5	2560-3600	GNSS deny

that when electromagnetic interference is imposed on the systems, the attitude and heading errors of the SINS/GPS integrated model become severely fluctuant. By contrast, the SINS/PNS/CNS integrated model and the SINS/PNS integrated model are not affected by the disturbance. At step 3 (1260s-2500s), although the disturbance disappears, the heading errors of the SINS/GPS integrated model are still not decreased. At step 5 (2560s-3600s), the satellite navigation signal is denied. The attitude and heading errors of the SINS/GPS integrated model are divergent over time, and the navigation performance is greatly decreased. For the test, the mean value of the attitude and heading errors of the SINS/GPS integrated model is 3.78°, which is larger than that of the SINS/PNS integrated model with 0.07° and the SINS/PNS/CNS integrated model with 0.02°. The standard deviation value of the attitude and heading errors of the SINS/GPS integrated model is also the largest one compared with that obtained by the SINS/PNS and the SINS/PNS/CNS integrated models.

The electromagnetic interference test results show that the SINS/GPS integrated model is vulnerable to electromagnetic interference environments. While the SINS/PNS/CNS integrated model is hardly affected by the electromagnetic interference under short-term electromagnetic interference or GNSS-denied conditions. Hence, the proposed integrated model can be as a backup system when the navigation system suffers from electromagnetic interference or GNSS-denied.

VI. CONCLUSION

In this paper, concerned with the challenge of attitude and heading determination of HALE UAVs in GNSS disturbed conditions, a bioinspired navigation strategy combined with polarized skylight and starlight is proposed. In combination with the DoP and e-vector information, a sun calculation method is presented, and the environmental adaptability of the polarization navigation system can be improved. In addition, the attitude and heading determination algorithm and the system integrated strategy are presented. The simulation results show that the proposed method can correct the attitude and heading errors of the inertial navigation system and have a better attitude and heading tracking performance. The merit of the method lies in its ability to work with only one star available, which is necessary for aircraft working in sky conditions in daytime. The method is suitable for electromagnetic interference environments or GNSS-denied conditions. In this paper, the measurement noises of the polarization sensor and star sensor are assumed as Gaussian, which may not be the cases in practical applications. Therefore, it requires further research in our future work.

APPENDIX

$\mathbf{R}_x(\theta)$, $\mathbf{R}_y(\gamma)$, and $\mathbf{R}_z(\psi)$ are the attitude transition matrix, and they can be expressed as:

$$\mathbf{R}_x(\theta) = \begin{bmatrix} 1 & 0 & 0 \\ 0 & \cos\theta & -\sin\theta \\ 0 & \sin\theta & \cos\theta \end{bmatrix}$$
$$\mathbf{R}_y(\gamma) = \begin{bmatrix} \cos\gamma & 0 & \sin\gamma \\ 0 & 1 & 0 \\ -\sin\gamma & 0 & \cos\gamma \end{bmatrix}$$
$$\mathbf{R}_z(\psi) = \begin{bmatrix} \cos\psi & -\sin\psi & 0 \\ \sin\psi & \cos\psi & 0 \\ 0 & 0 & 1 \end{bmatrix} \tag{A1}$$

The roll γ and the heading ψ can be calculated as:

heading ψ			roll γ		
C_{22}	C_{12}	ψ	C_{31}	C_{33}	γ
+	+	$\psi_m + 2\pi$	+	+	γ_m
+	-	ψ_m	-	+	
-		$\psi_m + \pi$	+	-	$\gamma_m - \pi$
0	+	$3\pi/2$	-	-	
0	-	$\pi/2$	+	-	$\gamma_m + \pi$

The matrix $z(t)$ and $\boldsymbol{H}(t)$ can be expressed as:

$$z(t) = \begin{bmatrix} \Delta\theta & \Delta\gamma & \Delta\psi \end{bmatrix}^T$$
$$\boldsymbol{H}(t) = \begin{bmatrix} \begin{bmatrix} -\cos\psi & -\sin\psi & 0 \\ \dfrac{\sin\psi}{\cos\theta} & -\dfrac{\cos\psi}{\cos\theta} & 0 \\ -\tan\theta\sin\psi & \tan\theta\cos\psi & -1 \end{bmatrix} 0_{3\times 12} \end{bmatrix} \tag{A2}$$

REFERENCES

[1] S. Wang, D. Ma, M. Yang, L. Zhang, and G. Li, "Flight strategy optimization for high-altitude long-endurance solar-powered aircraft based on gauss pseudo-spectral method," *Chin. J. Aeronaut.*, vol. 32, no. 10, pp. 2286–2298, Oct. 2019.
[2] A. Ali and N. El-Sheimy, "Low-cost MEMS-based pedestrian navigation technique for GPS-denied areas," *J. Sensors*, vol. 2013, Aug. 2013, Art. no. 197090.
[3] G. Flores, S. Zhou, R. Lozano, and P. Castillo, "A vision and GPS-based real-time trajectory planning for a MAV in unknown and low-sunlight environments," *J. Intell. Robotic Syst.*, vol. 74, nos. 1–2, pp. 59–67, Apr. 2014.
[4] X. Chen, C. Shen, W.-B. Zhang, M. Tomizuka, Y. Xu, and K. Chiu, "Novel hybrid of strong tracking Kalman filter and wavelet neural network for GPS/INS during GPS outages," *Measurement*, vol. 46, no. 10, pp. 3847–3854, Dec. 2013.
[5] G. T. Schmidt, "Navigation sensors and systems in GNSS degraded and denied environments," *Chin. J. Aeronaut.*, vol. 28, no. 1, pp. 1–10, Feb. 2015.
[6] D. A. Sigel and D. Wettergreen, "Star tracker celestial localization system for a lunar rover," in *Proc. IEEE/RSJ Int. Conf. Intell. Robots Syst.*, San Diego, CA, USA, Oct. 2007, pp. 2851–2856.
[7] K. Badshah, Q. Yongyuan, and J. Zhang, "SINS/CNS integration algorithm and simulations for extended time flights using linearized Kalman filtering," in *Proc. IEEE Int. Conf. Commun. Softw. Netw. (ICCSN)*, Chengdu, China, Jun. 2015, pp. 33–37.
[8] M.-L. Xie, X.-X. Yang, J.-F. Han, Y. Wei, P. Yue, X.-G. Deng, and W. Huang, "Research on the airborne SINS/CNS integrated navigation system assisted by BD navigation system," in *Proc. Sel. Papers Photoelectron. Technol. Committee Conf.*, Various, China, Nov. 2015, pp. 97961X-1–97961X-9.
[9] M. Nieuwenhuisen, D. Droeschel, M. Beul, and S. Behnke, "Autonomous navigation for micro aerial vehicles in complex GNSS-denied environments," *J. Intell. Robotic Syst.*, vol. 84, nos. 1–4, pp. 199–216, Dec. 2016.
[10] P. Berthold, "Genetic control of migratory behaviour in birds," *Trends Ecol. Evol.*, vol. 6, no. 8, pp. 254–257, 1991.
[11] W. Wiltschko and R. Wiltschko, "Magnetic orientation in birds," *J. Express Biol.*, vol. 199, no. 1, pp. 29–38, 1996.
[12] S. T. Emlen, "The stellar-orientation system of a migratory bird," *Sci. Amer.*, vol. 233, no. 2, pp. 102–111, Aug. 1975.
[13] J. Phillips and F. Moore, "Calibration of the sun compass by sunset polarized light patterns in a migratory bird," *Behav. Ecology Sociobiol.*, vol. 31, no. 3, pp. 189–193, Sep. 1992.
[14] H. Lu, K. Zhao, Z. You, and K. Huang, "Real-time polarization imaging algorithm for camera-based polarization navigation sensors," *Appl. Opt.*, vol. 56, no. 11, pp. 3199–3205, Apr. 2017.
[15] J. Chu, Z. Wang, L. Guan, Z. Liu, Y. Wang, and R. Zhang, "Integrated polarization dependent photodetector and its application for polarization navigation," *IEEE Photon. Technol. Lett.*, vol. 26, no. 5, pp. 469–472, Mar. 1, 2014.
[16] J. Yang, T. Du, B. Niu, C. Li, J. Qian, and L. Guo, "A bionic polarization navigation sensor based on polarizing beam splitter," *IEEE Access*, vol. 6, pp. 11472–11481, 2018.
[17] T. Du, X. Li, Y. Wang, J. Yang, and W. Liu, "Multiple disturbance analysis and calibration of an inspired polarization sensor," *IEEE Access*, vol. 7, pp. 58507–58518, 2019.
[18] J. Dupeyroux, J. R. Serres, and S. Viollet, "AntBot: A six-legged walking robot able to home like desert ants in outdoor environments," *Sci. Robot.*, vol. 4, no. 27, Feb. 2019, Art. no. eaau0307.
[19] R. Jin, H. Sun, J. Sun, W. Chen, and J. Chu, "Integrated navigation system for UAVs based on the sensor of polarization," in *Proc. IEEE Int. Conf. Mechatronics Autom.*, Harbin, China, Aug. 2016, pp. 2466–2471.
[20] W. Zhi, J. Chu, J. Li, and Y. Wang, "A novel attitude determination system aided by polarization sensor," *Sensors*, vol. 18, no. 2, p. 158, 2018.
[21] J. Yang, T. Du, X. Liu, B. Niu, and L. Guo, "Method and implementation of a bio-inspired attitude and heading reference system by integration of polarization compass and inertial sensors," *IEEE Trans. Ind. Electron.*, early access, Nov. 15, 2019, doi: 10.1109/TIE.2019.2952799.
[22] D. Lambrinos, H. Kobayashi, R. Pfeifer, M. Maris, T. Labhart, and R. Wehner, "An autonomous agent navigating with a polarized light compass," *Adapt. Behav.*, vol. 6, no. 1, pp. 131–161, Jun. 1997.
[23] D. Lambrinos, R. Möller, T. Labhart, R. Pfeifer, and R. Wehner, "A mobile robot employing insect strategies for navigation," *Robot. Auto. Syst.*, vol. 30, nos. 1–2, pp. 39–64, Jan. 2000.
[24] J. Chahl and A. Mizutani, "Biomimetic attitude and orientation sensors," *IEEE Sensors J.*, vol. 12, no. 2, pp. 289–297, Feb. 2012.
[25] X. Kong, W. Wu, L. Zhang, X. He, and Y. Wang, "Performance improvement of visual-inertial navigation system by using polarized light compass," *Ind. Robot, Int. J.*, vol. 43, no. 6, pp. 588–595, Oct. 2016.
[26] Y. Wang, X. Hu, L. Zhang, J. Lian, and X. He, "Polarized light compass-aided visual-inertial navigation under foliage environment," *IEEE Sensors J.*, vol. 17, no. 17, pp. 5646–5653, Sep. 2017.
[27] W. Quan, J. Li, X. Gong, and J. Fang, *INS/CNS/GNSS Integrated Navigation Technology*. Berlin, Germany: Springer, 2015.
[28] Y. Wang, J. Chu, R. Zhang, L. Wang, and Z. Wang, "A novel autonomous real-time position method based on polarized light and geomagnetic field," *Sci. Rep.*, vol. 5, no. 1, Sep. 2015, Art. no. 9725.
[29] G. Horváth, *Polarized Light and Polarization Vision in Animal Sciences*. Berlin, Germany: Springer, 2014.
[30] Z. Yang, J. Zhou, H. Huang, Y. Liu, and Z. Li, "Measuring solar vector with polarization sensors based on polarization pattern," *Optik*, vol. 141, pp. 147–156, Jul. 2017.
[31] Z. M. Gizatullin, M. G. Nuriev, and M. P. Shleimovich, "Physical modeling of electromagnetic interference in unmanned aerial vehicle under action of indirect lightning strike," in *Proc. Dyn. Syst., Mech. Mach. (Dyn.)*, Omsk, Russia, Nov. 2017, pp. 1–4.

QINGYUN ZHANG was born in Harbin, China, in 1990. He received the B.S. and M.S. degrees from the School of Mechanical Electronic and Information Engineering, China University of Miming and Technology, Beijing, China, in 2012 and 2015, respectively. He is currently pursuing the Ph.D. degree with the School of Automation Science and Electrical Engineering, Beihang University, Beijing. His research interests include bionic polarization navigation and autonomous integrated navigation systems.

JIAN YANG was born in Chifeng, China, in 1987. He received the B.S. degree from the Department of Automatic Control, Northeastern University, Shenyang, China, in 2011, and the Ph.D. degree from Beihang University, Beijing, China, in 2018. He holds a postdoctoral position at Beihang University. His current research interests include bionic polarization navigation, autonomous navigation systems, and filter design with their applications to aerospace.

XIN LIU was born in Dongying, China, in 1995. He received the B.S. degree from the School of Electronic Information Engineering, Inner Mongolia University, Huhhot, China, in 2017. He is currently pursuing the Ph.D. degree with the School of Automation Science and Electrical Engineering, Beihang University, Beijing, China. His research interests include bionic polarization sensor calibration and error compensation and bionic autonomous navigation systems.

LEI GUO (Senior Member, IEEE) was born in Qufu, China, in 1966. He received the B.S. and M.S. degrees from Qufu Normal University, Qufu, in 1988 and 1991, respectively, and the Ph.D. degree in control engineering from Southeast University, Nanjing, China, in 1997. He is currently a Professor with the School of Automation Science and Electrical Engineering, Beihang University, Beijing, China. He has authored or coauthored over 120 articles and one monograph. His research interests include robust control, stochastic systems, fault detection, filter design, and nonlinear control with their applications to aerospace systems.